The Astronomical Journal, 159:111 (13pp), 2020 March https://doi.org/10.3847/1538-3881/ab6a0b

Near-ultraviolet Transmission Spectroscopy of HD 209458b: Evidence of Ionized Iron Beyond the Planetary Roche Lobe

Patricio E. Cubillos[1], Luca Fossati[1], Tommi Koskinen[2], Mitchell E. Young[1], Michael Salz[3], Kevin France[4], A. G. Sreejith[1], and Carole A. Haswell[5]
[1] Space Research Institute, Austrian Academy of Sciences, Schmiedlstrasse 6, A-8042, Graz, Austria; patricio.cubillos@oeaw.ac.at
[2] Lunar and Planetary Laboratory, University of Arizona, 1629 E. University Boulevard, Tucson, AZ 85721, USA
[3] Hamburger Sternwarte, Universität Hamburg, Gojenbergsweg 112, D-21029 Hamburg, Germany
[4] Laboratory for Atmospheric and Space Physics, University of Colorado, 600 UCB, Boulder, CO 80309, USA
[5] School of Physical Sciences, The Open University, Walton Hall, Milton Keynes MK7 6AA, UK
Received 2019 April 30; revised 2020 January 7; accepted 2020 January 8; published 2020 February 17

Abstract

The inflated transiting hot Jupiter HD 209458b is one of the best studied objects since the beginning of exoplanet characterization. Transmission observations of this system between the mid-infrared and the far-ultraviolet have revealed the signature of atomic, molecular, and possibly aerosol species in the lower atmosphere of the planet, as well as escaping hydrogen and metals in the upper atmosphere. From a re-analysis of near-ultraviolet transmission observations of HD 209458b we detect ionized iron (Fe^+) absorption in a 100 Å-wide range around 2370 Å, lying beyond the planetary Roche lobe. However, we do not detect absorption of equally strong Fe^+ lines expected to be around 2600 Å. Further, we find no evidence for absorption by neutral magnesium (Mg), ionized magnesium (Mg^+), nor neutral iron (Fe). These results avoid the conflict with theoretical models previously found by Vidal-Madjar et al., which detected Mg but did not detect Mg^+ from this same data set. Our results indicate that hydrodynamic escape is strong enough to carry atoms as heavy as iron beyond the planetary Roche lobe, even for planets less irradiated than the extreme ultra-hot Jupiters such as WASP-12 b and KELT-9 b. The detection of iron and nondetection of magnesium in the upper atmosphere of HD 209458b can be explained by a model in which the lower atmosphere forms (hence, sequesters) primarily magnesium-bearing condensates, rather than iron condensates. This is suggested by current microphysical models. The inextricable synergy between upper- and lower-atmosphere properties highlights the value of combining observations that probe both regions.

Unified Astronomy Thesaurus concepts: Exoplanet atmospheres (487); Transmission spectroscopy (2133); Radiative transfer (1335)

1. Introduction

The early G-type star HD 209458 hosts what is considered to be the prototypical hot Jupiter. The ∼0.7 Jupiter-mass planet has an inflated atmosphere, an orbital period of about 3.5 days, and an equilibrium temperature of about 1500 K (Knutson et al. 2007). HD 209458 is among the five brightest and nearest stars known to host a transiting hot Jupiter (see, e.g., Edwards et al. 2019). In addition, HD 209458b was the first exoplanet detected in transit (Charbonneau et al. 2000) and the first for which an atmosphere was detected (Charbonneau et al. 2002). Consequently, HD 209458b has been one of the most studied hot Jupiters to date with transmission and emission observations obtained from space and ground. These observations led to the detection of planetary atmospheric signatures ranging from the far-ultraviolet (FUV) to infrared bands.

Shortly after the first detection of the atmosphere of HD 209458b at the position of the Na D lines (Charbonneau et al. 2002), Vidal-Madjar et al. (2003) reported the detection of an extended hydrogen envelope surrounding the planet. This result was based on primary transit observations obtained with the *Hubble Space Telescope* (*HST*) at FUV wavelengths, which revealed a ∼10% deep absorption in the wings of the Lyα line (the core of the Lyα line is completely absorbed by the interstellar medium; see also Ben-Jaffel 2007; Vidal-Madjar et al. 2008). The strength of the Lyα absorption signature indicated the presence of escaping atomic hydrogen outside the planet's Roche lobe. This first discovery inspired the development of a number of computational models aiming at describing the physical mechanisms of exoplanet atmospheric escape (e.g., Lammer et al. 2003; Yelle 2004; García Muñoz 2007; Murray-Clay et al. 2009; Bourrier & Lecavelier des Etangs 2013; Koskinen et al. 2013a, 2013b; Kislyakova et al. 2014; Salz et al. 2015; Carroll-Nellenback et al. 2017; Khodachenko et al. 2017; Debrecht et al. 2018; Kubyshkina et al. 2018) and the effort to look for signatures of escape around other close-in planets and at different wavelengths. In fact, further UV observations led to the detection of escaping atmospheres around the hot Jupiters HD 189733b in the FUV (e.g., Lecavelier des Etangs et al. 2012), WASP-12 b in the near-ultraviolet (NUV; e.g., Fossati et al. 2010; Haswell et al. 2012, and indications for WASP-121 b in the NUV (Salz et al. 2019), and the warm Neptunes GJ 436 b and GJ 3470b in the FUV (e.g., Ehrenreich et al. 2015; Bourrier et al. 2018).

The hot Jupiter HD 209458b has since been observed at both FUV and NUV wavelengths, to further study atmospheric escape. The FUV observations focused mostly on detecting planetary atmospheric absorption at the position of resonance lines of abundant elements, particularly C, O, and Si. The observations led to the detection of O and C^+ escaping from the planet (Vidal-Madjar et al. 2004; Linsky et al. 2010; Ballester & Ben-Jaffel 2015), while the detection of Si^{2+} is still controversial (Linsky et al. 2010; Ballester & Ben-Jaffel 2015).

1.1. NUV Atmospheric Characterization of HD 209458b

Vidal-Madjar et al. (2013) presented the results of three *HST* transit observations conducted at NUV wavelengths. Observing

exoplanetary atmospheric escape in the NUV has some key advantages over the FUV (Haswell et al. 2012; Fossati et al. 2015; Haswell 2018): (1) for K-type stars and earlier, the NUV stellar emission is dominated by the photospheric continuum, which has a significantly higher flux than that the FUV emission lines, thus improving the signal-to-noise (S/N); and (2) because it is dominated by photospheric emission, the background over which a transit is observed is more homogeneous and less affected by bright/dark spots typical of the FUV chromospheric emission (see, e.g., Haswell 2010; Llama & Shkolnik 2015, 2016). In addition, the NUV spectral range contains a large number of resonance lines of abundant metals (e.g., Mg, Fe, and Mn), some of which have been detected in escaping exoplanetary atmospheres (e.g., Fossati et al. 2010; Haswell et al. 2012; Sing et al. 2019).

Vidal-Madjar et al. (2013) reported the detection of planetary Mg absorption at 2.1σ level with Doppler velocities ranging between -62 and $-19\,\mathrm{km\,s^{-1}}$ away from the position of the Mg 2853 Å resonance line. Vidal-Madjar et al. (2013) and Bourrier et al. (2014, 2015) interpreted this as evidence of planetary Mg atoms escaping the planet's atmosphere and moving away from its host star, accelerated by radiation pressure. Vidal-Madjar et al. (2013) also looked for Mg^+ absorption at the position of the Mg^+ *h* and *k* resonance lines at about 2800 Å, but without success. In addition, they binned the whole available spectral window to 200 Å bins looking for the rise of the planetary radius with decreasing wavelength due to Rayleigh scattering, but the data quality was not high enough to constrain the Rayleigh slope.

The low ionization potential of Mg (7.65 eV) implies that radiation at wavelengths shorter than ∼1621 Å is capable of ionizing the atom. Since the photospheric continuum of the G-type star HD 209458 starts rising near 1450–1500 Å (Vidal-Madjar et al. 2004; France et al. 2010), the detection of Mg and not of Mg^+ came as a great surprise. Vidal-Madjar et al. (2013) explained this as due to electron recombination depleting Mg^+ and enhancing Mg in the atmosphere and derived a minimum electron density of $10^{8–9}\,\mathrm{cm^{-3}}$ required to achieve this. This electron density is about a factor of 10 higher than the peak electron density predicted by upper atmosphere models ($10^{7–8}\,\mathrm{cm^{-3}}$; Koskinen et al. 2013a, 2013b; Lavvas et al. 2014).

Furthermore, Bourrier et al. (2014) found that the best-fit electron density required to match the observations is even higher, at about $10^{10}\,\mathrm{cm^{-3}}$. In addition to being significantly higher than theoretical predictions, their estimate of the Mg^+ recombination rate seems to assume that all available electrons are used to recombine Mg^+. Since this is unrealistic, we infer that for recombination to explain the detection of Mg and the nondetection of Mg^+, the required electron density must therefore be even larger than $10^{10}\,\mathrm{cm^{-3}}$.

Motivated by these considerations, we present a re-analysis of the *HST* NUV observations of HD 209458b. The primary aims of this work are to re-investigate the detection and nondetection of the Mg and Mg^+ absorption, respectively, search for metal absorption lines in the entire Space Telescope Imaging Spectrograph (STIS) NUV spectrum, and attempt to reconcile the observations with theory. In Section 2, we describe the observation in more detail. In Section 3, we describe our data-analysis methodology. In Section 4, we provide a theoretical interpretation of the observations. In Section 5 we discuss the main implications of our analysis and compare our results to those of Vidal-Madjar et al. (2013). Finally, we summarize our conclusions in Section 6.

2. Observations

We re-analyze the three archival NUV transmission observations of the planetary system HD 209458, obtained with *HST*, using STIS (program #11576; Vidal-Madjar et al. 2013), the NUV Multi-Anode Microchannel Array detector, and E230M grating. Each transit observation (one *HST* visit) consists of five consecutive *HST* orbits, where each *HST* orbit lasts about 90 minutes. For each visit, the first two and last *HST* orbits occur out of transit, the third orbit during the transit ingress, and the fourth orbit shortly after the mid-transit time. Each orbit consists of 10 consecutive exposures (frames) of 200 s each, except for the first orbit, which consists of nine frames to accommodate acquisition observations. Each frame consists of an echelle spectrum comprising 23 orders, in which each order consists of 1024 wavelength samples, with a resolving power of $\lambda/\Delta\lambda = 30{,}000$, and approximately two pixels per resolution element (where the resolution element is approximately 10 $\mathrm{km\,s^{-1}}$, or equivalently, 0.09 Å). The entire STIS spectrum covers the 2300–3100 Å range, with some overlap between the orders.

3. Data Analysis

We follow the standard procedure for extracting the planetary transit signature from time-series observations. We start the analysis from the CALSTIS[6] (version 3.4) reduced and extracted spectra, which have been corrected for flat field, extracted, corrected for background emission, and wavelength and flux calibrated. Our analysis is based on the flux calibrated spectra and their uncertainties, which account for photon noise and uncertainties on flat fielding and flux calibration. We exclude the first orbit from each visit and the first frame from each orbit, since they show severe systematics that we were not able to correct for.

In the following sections we describe our analysis, in which we adopt a two-step approach. First, we characterize instrumental systematics using wavelength-integrated data (white-light analysis). Second, we obtain wavelength-resolved transmission spectra from the data that have been corrected for systematics (spectral analysis).

3.1. White-light Analysis

In this step, we integrate the flux over each echelle spectral order to increase the S/N, and then detrend the astrophysical signal from the instrumental systematics. We begin by masking bad data points based on three criteria: first, as stated above, we exclude the first orbit from each visit and the first frame from each orbit; second, we exclude data points with abnormally low uncertainties, i.e., an order of magnitude lower than the median uncertainties (typically, a handful of data points at the edges of the echelle order for each frame); and third, we use the overlap between the echelle orders to exclude data points where the fluxes differ from each other by more than 5σ. Overall, this bad-pixel-masking procedure removes typically five pixels at each end of the echelle order, for each frame. We then produce

[6] http://www.stsci.edu/hst/stis/software/analyzing/calibration/pipe_soft_hist/intro.html

the raw white light curves by summing the flux over each spectral order and propagating the uncertainties accordingly.

We fit the raw light curves with parametric transit and systematics models as a function of time (t) and wavelength (λ):

$$F(t, \lambda) = F_s T(t, \lambda) S(t, \lambda), \quad (1)$$

where F_s is the out of transit flux, $T(t, \lambda)$ is a Mandel & Agol (2002) transit model, and $S(t, \lambda)$ is a model of the instrumental systematics. To obtain statistically robust parameter estimations, we apply a Levenberg–Marquardt optimization to compute the best-fit parameters, and a Markov Chain Monte Carlo (MCMC) algorithm to compute the parameter credible intervals. To this end, we use the open-source MC3 Python package[7] (Cubillos et al. 2017). For the MCMC exploration, we select the Snooker Differential-evolution MCMC sampler (ter Braak & Vrugt 2008).

Except for the transit epoch, we fix the orbital parameters to the values measured at optical wavelengths, since they are more precise than those we can infer from the NUV data. We assume an orbital period of $P = 3.5247486$ days (Knutson et al. 2007), an orbital inclination of $i = 86.^{\circ}66$, and a semimajor axis to stellar radius ratio of $a/R_s = 8.7947$ (Hayek et al. 2012). These values fit the NUV data well. Given the gaps in the *HST* observations, adopting different orbital-parameter values from the literature does not significantly impact our results as they impact mostly the timing of the transit light curve rather than the relative depths as a function of wavelength, (see, e.g., further discussion in Evans et al. 2018).

For each order, we compute the four-coefficient nonlinear limb-darkening coefficients (as defined in Claret 2000) using the open-source routines of Espinoza & Jordán (2015), which we keep fixed during the fit. For this calculation, we consider the PHOENIX stellar model that most closely matches the physical properties of HD 209458 (effective temperature $T_{\rm eff} = 6000$ K, surface gravity $\log g = 4.5$, and solar elemental metallicity). Although fixing the limb-darkening coefficients (instead of fitting) is not optimal, the low S/N and the sparse coverage of the NUV transit light curve does not allow us to constrain the coefficients sufficiently well. Therefore, the transit depth and out-of-transit flux remain the only astrophysical fitting parameters.

In addition to the astrophysical signal, we simultaneously fit the *HST* instrumental systematics. *HST* time-series observations show well-known systematics that affect the different instruments and observing modes on board (e.g., Wakeford et al. 2016; Alam et al. 2018; Sing et al. 2019): the "breathing" effect, which varies with the *HST* orbital period, and visit-long trends. We model these systematics considering a family of polynomial curves as in Vidal-Madjar et al. (2013):

$$\begin{aligned} S(t, \phi) = 1 &+ a_1(t - t_0) + a_2(t - t_0)^2 \\ &+ b_1(\phi - \phi_0) + b_2(\phi - \phi_0)^2 \\ &+ b_3(\phi - \phi_0)^3 + b_4(\phi - \phi_0)^4, \end{aligned} \quad (2)$$

where ϕ are the *HST* orbital phases; a_i and b_i are fitting parameters for the visit-long and breathing systematics, respectively; and t_0 and ϕ_0 are a fixed reference time and phase. We set $t_0 = T_0(t)$ and $\phi_0 = 0.2$, the transit mid-time and *HST* mid-phase of the observations, respectively, to minimize correlations between the polynomial coefficients. The expression shown in Equation (2) is the most complex form of $R(t, \phi)$ we considered, as we tested all possible lower-order polynomial expressions in t and ϕ.

[7] https://mc3.readthedocs.io/

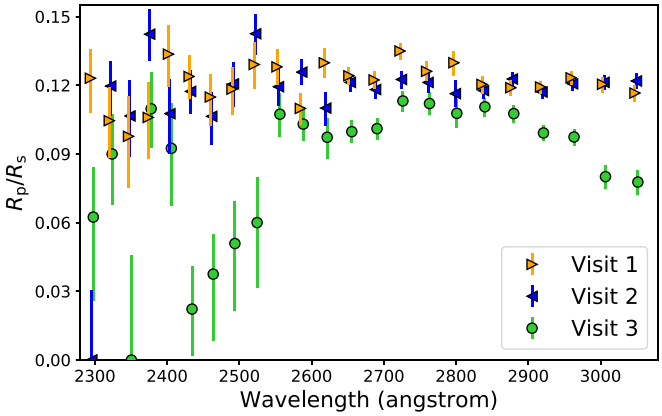

Figure 1. HD 209458b white-analysis transmission spectra. Each data point shows the best-fitting systematics-corrected radius ratio for the echelle orders of each visit (see the legend). The error bars denote the 68% highest-posterior-density credible region (1σ uncertainty).

Table 1
BIC Model Comparison

Polynomial Degree (t, ϕ)	BIC Visit 1	Visit 2	Visit 3
1, 1	1495.2	1952.0	2164.4
1, 2	1546.0	2042.9	2301.0
1, 3	1656.4	2142.5	2276.7
1, 4	1783.9	2282.5	2377.6
2, 1	1623.6	1974.4	2196.6
2, 2	1674.1	2053.5	2334.0
2, 3	1784.6	2147.8	2308.9
2, 4	1912.0	2287.7	2408.5

We fit the light curves testing each combination of polynomial degree in t and ϕ, selecting the preferred model by minimizing the Bayesian information criterion (BIC), $\mathrm{BIC} = \chi^2 + k \log N$, where k is the number of free parameters and N is the number of data points. Table 1 shows the results of the Bayesian model selection. For all visits, the BIC prefers linear polynomials in t and ϕ.

Figure 1 shows the best-fitting transit depth for each visit and spectral order from the white-light analysis, for the preferred systematics model in Table 1. The Appendix section presents the order-by-order and visit-by-visit light curves. As in Vidal-Madjar et al. (2013), the transit depths of the first two visits agree well with each other and show a nearly constant transit depth with wavelength. In contrast, the third visit shows strong anomalous systematics of unknown origin that corrupt the transit fit, producing wide variations in transit depth across the spectrum. Thus, as done by Vidal-Madjar et al. (2013), we discard the results from the third visit from further analyses.

3.2. Spectral Analysis

In this step, we divide the data into several spectral channels to search for wavelength-dependent features in the transmission spectra. The main complication of the analysis is choosing the appropriate width of the wavelength channels. On the one

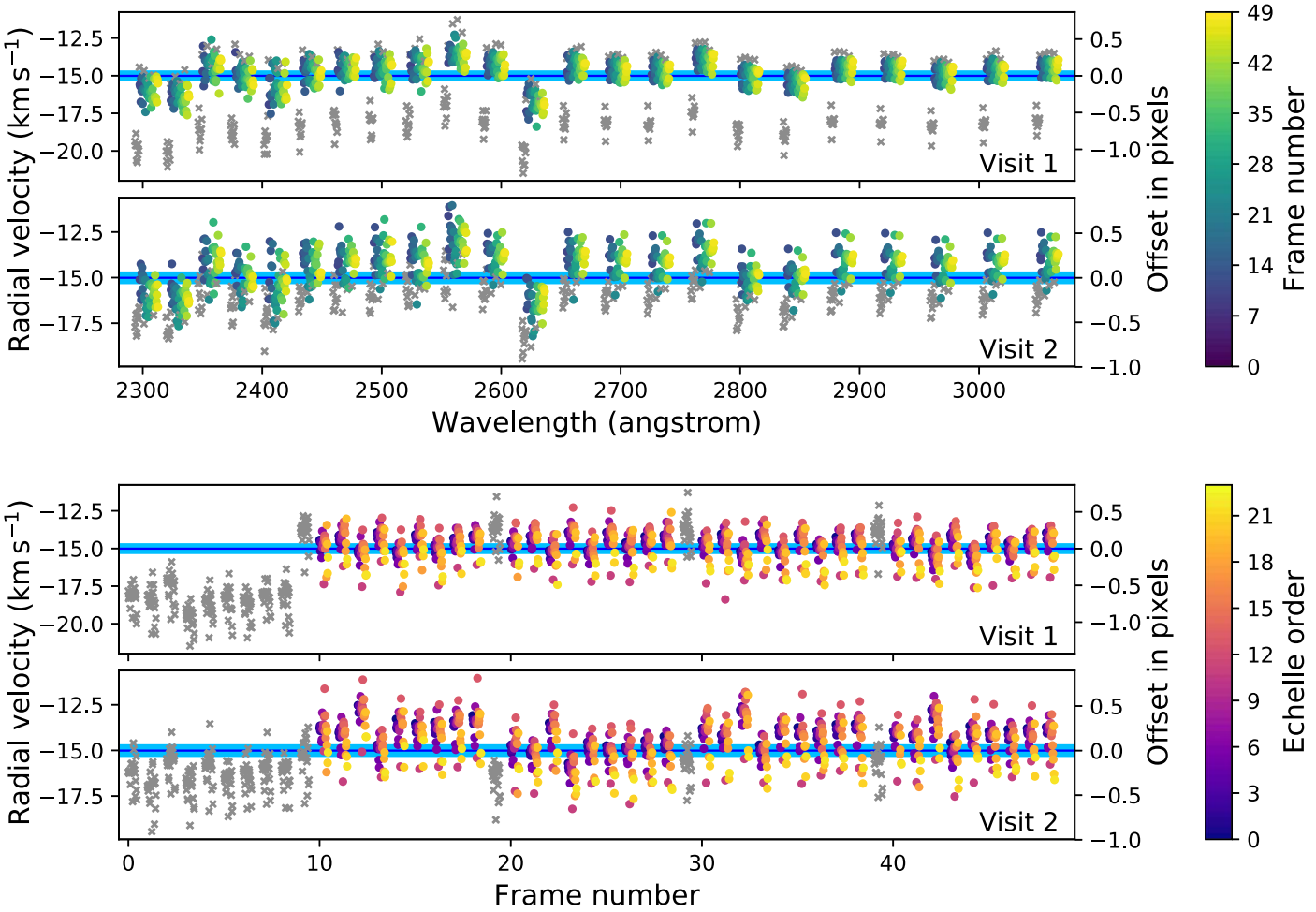

Figure 2. Wavelength calibration of each observed spectra as a function of wavelength (top two panels) and as a function of frame number (bottom two panels) for the first and second *HST* visit. The colored dots denote the valid frames used for the fit, color coded by frame number (top two panels) and by spectral order (bottom two panels); the gray crosses denote the discarded frames (first *HST* orbit and first frame of each *HST* orbit). The horizontal dark and light blue lines denote the systemic radial velocity of -15.01 ± 0.29 km s^{-1} (Gaia Collaboration 2018). The markers have been slightly shifted horizontally for better visualization.

hand, the expected NUV features are narrow absorption lines a few km s^{-1} wide, but narrow wavelength channels do not provide sufficient S/N to distinguish such features. On the other hand, broader channels build up S/N, but dilute the signal of potential spectral features. We thus analyze the data at four different spectral resolutions (25, 50, 100, and 1000 km s^{-1}) to assess this trade-off. A posteriori, we found that the data show isolated absorption features that get quickly diluted as one lowers the resolution. Therefore, our main conclusions rely on the highest-resolution analysis at 25 km s^{-1}, aided by the coarse 1000 km s^{-1} analysis as a continuum.

3.2.1. Wavelength Correction

We begin the spectral analysis by reading and masking the raw light curves as in the white-light analysis. To account for possible wavelength distortions of the spectra during a visit, we calibrate and correct the wavelength solution of each echelle order in each frame, with respect to the stellar rest frame. As a reference spectrum, we use a high-resolution line-by-line stellar photospheric emission model of HD 209458, computed with the 1D plane-parallel stellar atmosphere code of Shulyak et al. (2004). We find the wavelength correction for each order from the peak of the cross-correlation function between the Doppler-shifted data and the reference stellar spectrum.

Once calibrated, we Doppler-shift all light-curve frames of a given echelle order to a common wavelength solution using a cubic spline interpolation, and renormalizing the flux level to conserve the total flux in each frame. Since the flux uncertainties are Poison-noise dominated, we also use a cubic spline to estimate the uncertainties. To minimize the impact of the interpolation, we select as a reference point the frame that minimized the geometric mean of the shifts (of all the frames in a given order). As a result, 68% of the shifts are smaller than an eighth of a pixel. We remark that the wavelength correction is done order by order, thus it does not affect the total flux of each order, though the interpolation modifies the flux in each pixel, thus it affects the light curves of the narrow spectral channels. Figure 2 shows the relative Doppler shift between the individual orders for each frame and visit. The wavelength calibration shows significant shifts of nearly one pixel during a visit that varies systematically with the visit-long frame number, *HST*-orbit-long frame number, and echelle order. Furthermore, each visit shows a distinct Doppler-shift pattern.

3.2.2. Divide-white Systematics Correction

Following Kreidberg et al. (2014), we adapted their *HST*/WFC3 "divide-white" spectral analysis to the *HST*/STIS NUV data set. This is a two-step approach that uses the results from

the white-light analysis to remove the instrumental systematics from the raw spectral light curves (hence, the "divide-white"). Here, we construct a nonparametric systematics model by dividing the white-light curve by its best-fit order-by-order and visit-by-visit transit model, and normalizing the resulting quotient. Assuming that the instrumental systematics vary weakly with wavelength (an appropriate assumption for *HST* instruments; Alam et al. 2018), we divide the systematics model from each spectral light curve. The resulting light curves should then be dominated by the astrophysical transit signal.

We estimate uncertainties of the best-fit white transit model from the standard deviation of the distribution for the white-light transit model, generated from the white-analysis posterior distribution. Then we use the error-propagation formula (see, e.g., Bevington & Robinson 2003) to account for all uncertainties throughout the steps involved to construct the nonparametric systematics model and obtain the systematics-corrected light curve.

Once we have obtained the wavelength- and systematics-corrected light curves, we bin the data to a wavelength array with a constant resolution, where for each spectral channel, we co-add all flux contributions from the two visits and from all echelle orders (in regions of overlapping orders) and propagate the errors accordingly.

3.2.3. Transmission-spectrum Extraction

To derive robust estimates of the transmission spectrum, we apply two independent approaches to analyze the spectral light curves. In our first approach, we proceed in a similar manner as for the white-light analysis: we fit a Mandel & Agol (2002) transit model to the systematics-corrected spectral light curves in an MCMC run. As done previously, we fix the transit epoch, the orbital inclination, and ratio between the orbital semimajor axis and stellar radius (a/R_s). We also compute and fix the nonlinear limb-darkening coefficients for each spectral channel. Therefore, we fit for the transit depth and out-of-transit flux level in each spectral channel. Since the light curve combines data from different epochs, we fit the out-of-transit flux level of each visit with an individual free parameter. This approach produces statistically robust transit-depth estimates and maximizes the S/N; however, the results are influenced by the assumed limb-darkening coefficients.

As a second approach, we replicate the procedure of Vidal-Madjar et al. (2013), computing the absorption depth (AD) from the ratio between the total flux of the in-transit and out-of-transit *HST* orbits,

$$\mathrm{AD}(\lambda) = 1 - \frac{F_3 - F_4}{F_2 - F_5}, \tag{3}$$

where F_i represents systematics-corrected flux summed over the ith *HST* orbit, from both visits, within a spectral channel at wavelength λ. We propagate the errors according to Equation (3) to obtain the uncertainties, as done in Vidal-Madjar et al. (2013).

The transit depths from the AD(λ) and light-curve fit analyses should be similar, although we expect systematic variations. Since some data points in F_3 and F_4 occur during transit ingress and egress, the AD depths are expected to be lower than the light-curve fit depths. Additionally, the AD analysis does not account for stellar limb darkening. Nevertheless, we find a good agreement between the transit depths obtained from the light-curve fit and the AD method (see, e.g., Figure 5). Both methods produce similar uncertainties, and their transit-depth values agree within 1σ of each other for most spectral channels.

4. Atmospheric Signatures

Both spectral analyses of the HD 209458b NUV observations suggest that the planet has a nearly flat transmission spectrum. The high-resolution analyses show scattered absorption features across the spectrum; however, the limited S/N of the data complicates the detection of individual features. Here, we describe the analysis carried out to detect atmospheric features and discuss their physical interpretation.

4.1. Identification of Absorption Lines

The high-resolution transmission spectrum of HD 209458b (i.e., at 25 km s^{-1}) shows a large number of data points that deviate significantly above the continuum (i.e., the low-resolution spectrum at 1000 km s^{-1}). While from a normal distribution of 3600 data points one expects ~10 outliers deviating more than 3σ above and below the mean, we typically find ~25 data points deviating above the continuum by more than three times their uncertainty, suggesting that most of them are likely absorption features rising from the planetary atmosphere.

To determine whether we can associate these outliers to a particular atomic absorption line, we apply the probabilistic approach of Haswell et al. (2012). Using the Vienna Atomic Line Database (VALD) for the atomic line transitions (Piskunov et al. 1995) and adopting solar elemental abundances (Asplund et al. 2009), we collect all known atomic line transitions within a given wavelength range ($\Delta\lambda$) around each candidate absorption feature (i.e., outlier) lying at wavelength λ_0. To each known line transition i at wavelength λ_i we assign a "match" probability based on their proximity to λ_0, elemental abundance (n_j), and line strength (determined by the values of the transition probability gf_i, by the energy of the lower level $E^i_{\rm low}$ (in cm^{-1}) of the transition, and by the temperature of the atmospheric layers probed by the observations T) as

$$P'_i = \frac{|\lambda_i - \lambda_0|}{\Delta\lambda}\, n_j\, gf_i\, \exp\left(\frac{-hcE^i_{\rm low}}{kT}\right), \tag{4}$$

where h and k are respectively Planck's and Boltzmann's constants, and c is the speed of light. Finally, we normalize all match probabilities to obtain a discrete probability distribution: $P_i \equiv P'_i / \sum P'_i$. Thus, by finding the line transitions with a high match probability ($P_i > 68.3\%$, in this case), this framework reveals how likely it is for a specific line transition to be the unambiguous source of one of the 3σ outliers. Here, we consider a window of $\Delta\lambda = 2.5$ Å, which corresponds to a velocity of about 275 km s^{-1}, and adopt an atmospheric temperature of $T = 10{,}000$ K (e.g., Koskinen et al. 2013a).

We find that many of the outliers in the HD 209458b NUV data can be associated with Fe^+ absorption lines, at the $P_i > 68.3\%$ level, three outliers can be associated with Fe, and one with Mg^+. Figure 3 shows the derived transmission spectrum at a resolution of 25 km s^{-1} highlighting the position of the deviating data points, further associating them with the identified line transitions. On the top of each panel, we mark the positions of other lines of the Fe, Fe^+, and Mg^+ ions that

should be stronger than the identified ones. Note that this analysis implicitly assumes local thermodynamic equilibrium (LTE), while non-LTE effects are expected to play a significant role in the atmospheric layers probed by the observations. Therefore, the marks on the top of each panel in Figure 3 should be considered to be only indicative.

Figure 3 further compares the observed transmission spectrum to a theoretical model spectrum of HD 209458b (see Section 4.2). As expected from the line-identification analysis, many Fe^+ lines present in the model spectrum correlate with the location of outliers identified as Fe^+ features by the probabilistic approach presented above.

Since our high-resolution binning of 25 km s^{-1} is larger than the instrumental resolving element (10 km s^{-1}, the span of two pixels), there is an arbitrariness in the selection of the bin edges. Therefore, to confirm the robustness of our detections, we repeated the line-identification analysis four more times, shifting the bin locations by half the instrumental resolving element each time (i.e., a total of five iterations shifted by 5 km s^{-1} from each other); this is similar to the analysis of Spake et al. (2018). In Figure 3 we use a different symbol to mark the 3σ outliers at each shift. The colored markers denote the lines identified at multiple shifts, whereas the dark gray markers denote the lines identified at a single shift location.

The most robust features that we detect are a set of absorption features between 2330 and 2420 Å, consistent with a Fe^+ band. Most of these features appear at three or more different shifts, reassuring us that these are not artifacts resulting from the data analysis. We also find a large number of unknown absorption features. Note that by unknown, we do not mean that there are no known line transitions at the location of the outlier, rather that there is no unique line transition unambiguously associated with the observed feature. We do not detect any 3σ outliers near the Mg line at 2850 Å. The Mg^+ doublet at 2800 Å is interesting, because we only find a recurring absorption feature redward of the Mg^+ *h* line, but not near the Mg^+ *k* line. This is conflicting, since the two magnesium lines have similar strengths (Mg^+ *h* being slightly weaker), and thus the data should show both features. Given that we observe a Mg^+ *h* feature only at two shifts, and that we do not detect any feature around the Mg^+ *k* line, we conclude that this does not constitute a robust detection of magnesium.

4.2. Atmospheric Modeling

Here, we simulate theoretical transmission spectra of HD 209458b to compare against the observed spectra. We adopt the atmospheric properties (pressure, temperature, and radius) from existing models of HD 209458b and assume solar abundances for heavy elements. For the lower atmosphere, we use the dayside temperature–pressure profile from Showman et al. (2009). For the upper atmosphere (Figure 4), we couple the lower-atmosphere profile to the model of Koskinen et al. (2013a). We then use the spectral-synthesis and radiative-transfer code CLOUDY (version 17, Ferland et al. 2017) to calculate ion densities for a static atmosphere and the resulting transmission spectrum, including the parent neutral species of H, H_2, He, Na, Mg, and Fe in the model (Figure 3).

As the computation of the synthetic transmission spectrum with CLOUDY is yet to be published (M. E. Young et al. 2020, in preparation), we summarize the procedure here. Starting from the radial 1D planetary atmosphere model, we map the altitude, temperature, and abundance profiles onto concentric, spherically symmetric shells. Next, we define an array of parallel transmission rays, along the star–observer line of sight, as a function of the planetary impact parameter. Then, we track when each ray crosses each atmospheric layer of the planet to determine the temperature and composition along the ray path. We feed these ray profiles into CLOUDY to produce individual transmission spectra for each ray. Finally, we compute the total integrated transmission spectrum as the sum of the individual spectra, weighted by the annular area at the given impact parameter, assuming azimuthal symmetry around the terminator. We set the density profiles to zero at the Roche-lobe boundary because 1D atmospheric profiles are not valid above it. Therefore, the predicted strength of the absorption for the lines reaching the Roche-lobe boundary should be considered to be a lower limit, as the model itself clearly indicates substantial escape beyond the Roche lobe. We note that CLOUDY includes an extensive database of line transitions and includes options for both LTE and non-LTE level populations.

The key assumption of this work is that heavy magnesium and iron atoms with their ions are dragged along by the escaping lighter hydrogen atoms and protons so that they have roughly solar abundances in the upper-atmosphere part of the CLOUDY model. We used the escape model of Koskinen et al. (2013a) to validate this assumption for magnesium (Figure 4). This model does not currently include iron, a much more complex species, but the mass-loss rate from HD 209458b is predicted to be sufficiently high to mix iron to high altitudes where CLOUDY is used to calculate its ionization balance and transmission in Fe and Fe^+ lines. For magnesium, we show transmission based on the density profiles predicted by the escape model in Figure 5. We note that outflow can alter the ionization balance of metal absorbers and, in particular, enhance absorption by neutrals, whereas the current version of CLOUDY assumes a static atmosphere when calculating the ionization balance. Therefore, it will eventually also be necessary to study the escape of iron in detail and our modeling results in Figure 3 should be treated with some caution, although we consider them perfectly sufficient for a preliminary interpretation of observations.

5. Results

The model continuum, based on H_2 and He Rayleigh scattering, is consistent with the observed baseline (Figure 3), though the scatter does not allow the Rayleigh slope to be constrained.

This data alone does not allow us to distinguish between a clear or cloudy atmosphere. Doing this would require additional NUV observation, a broader wavelength coverage, or both. We will address this issue from a theoretical point of view in a future work. From the optical and infrared observations, it is still under debate whether HD 209458b has a cloudy or partially cloudy atmosphere (e.g., Deming et al. 2013; Madhusudhan et al. 2014; Sing et al. 2016; MacDonald & Madhusudhan 2017; Pinhas et al. 2019). We acknowledge that the NUV continuum may also include molecular absorbers (e.g., Evans et al. 2018) below the noise level, but the data do not support the detection of any such absorber.

In line with its low ionization potential, Mg in our models is ionized near the 1 μbar pressure level (see Figure 1 in Koskinen et al. 2014), so that Mg^+ and Fe^+ are the dominant magnesium and iron ionization states in the upper atmosphere. This is comparable, for example, with the detection of ionized

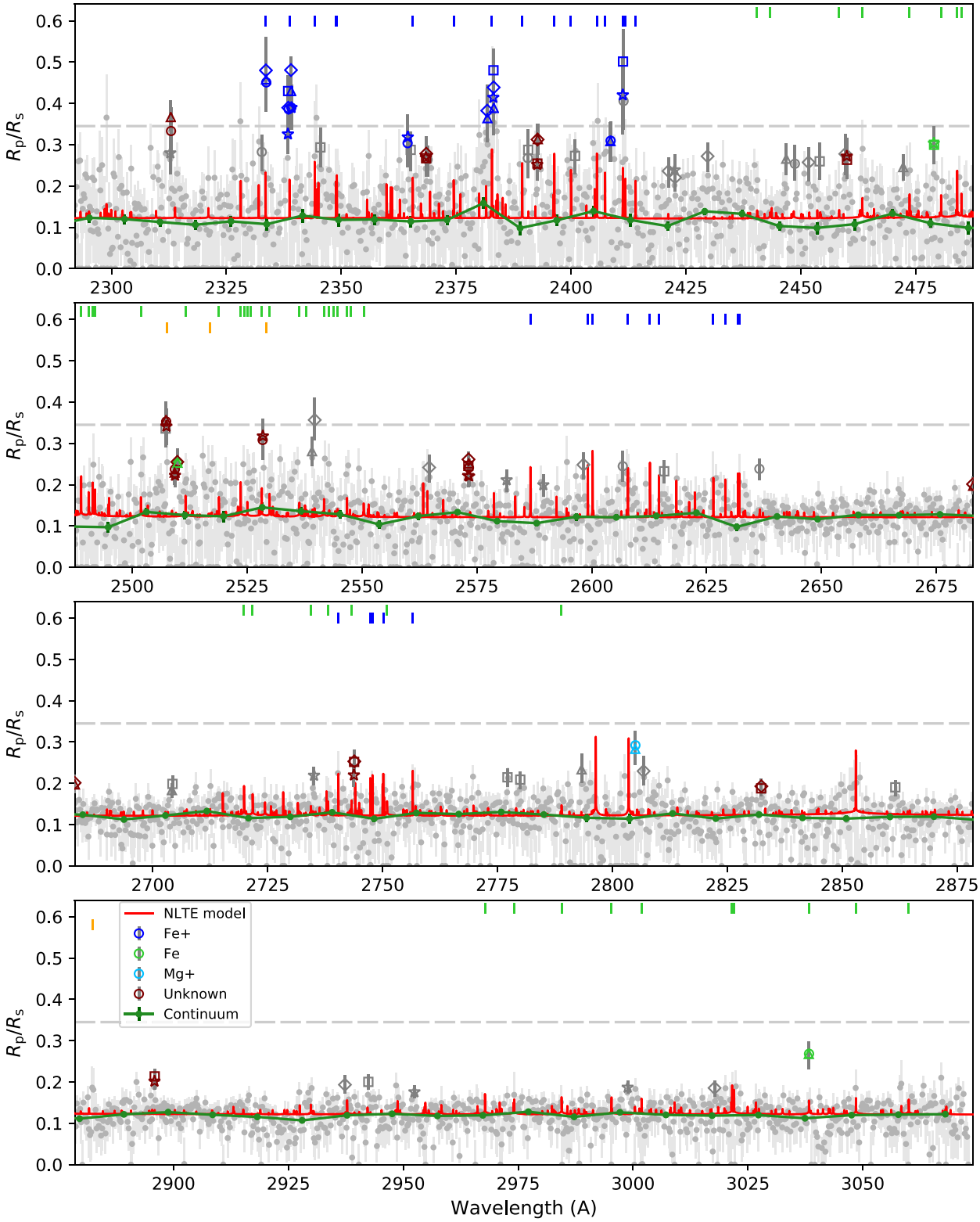

Figure 3. HD 209458b NUV transmission spectrum with outlier absorption features marked. The gray dots with error bars denote the observed spectrum at a resolution of 25 km s^{-1} and their 68% highest-posterior density credible intervals. The green dots with error bars connected by a solid line denote the observed spectrum at a resolution of 1000 km s^{-1}, which we adopted as the continuum baseline. The circle, star, square, diamond, and triangle markers with error bars denote the 3σ outliers at each of the shifts (see the text). The colored (see the legend) makers denote the outliers that were identified multiple times at the different shifts, whereas the dark gray markers denote the outliers identified at only one shift. The red curve denotes the theoretical model for this planet at infinite resolution (see Section 4.2 for details). The vertical-line marks at the top denote all line transitions for a given ion, with line strengths larger than the detected features in the data (same color code as in the legend). We also marked in orange the four strongest Si line transitions at 2510–2530 and 2880 Å, since they lay close to two absorption features, though our algorithm cannot uniquely associate them to Si. The horizontal dashed line denotes the size of the Roche lobe in the direction perpendicular to the line of sight (i.e., as probed by transmission spectroscopy).

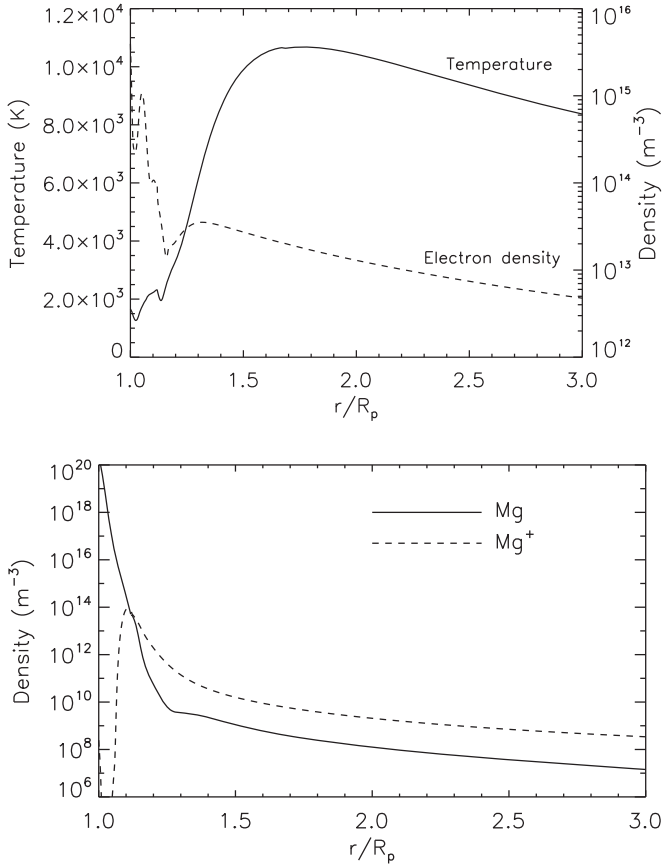

Figure 4. HD 209458b model atmospheric profiles for the temperature and electron density (top panel), and the magnesium number density (bottom panel). The profiles here extend from the 1 bar level to the Roche-lobe boundary ($r \approx 3R_p$). Since the sound speed barrier is crossed around the Roche lobe surface, these profiles are causally separated from the space above, and thus, unaffected by the physics above the Roche lobe. Extending the 1D model profiles beyond the Roche lobe would overestimate the number density, due to lack of 3D effects in our model; the densities should probably decrease faster with distance from the planet. Therefore we capped the densities at the Roche lobe to produce the transmission spectrum model shown in Figure 3.

magnesium and iron in the lower ionosphere of the Earth (Plane et al. 2015).

Figure 5 compares the magnesium absorption signatures predicted by our escape model with our transmission spectra of HD 209458b for the resonant Mg^+ h and k lines at about 2800 Å and the Mg line at about 2850 Å. In this figure, the curve shows the model spectra where the abundances extend beyond the Roche lobe. This is an overestimation, because it does not account for the asymmetric 3D distribution of the material beyond the planet's Roche lobe. If the planet had a magnesium overflow beyond the Roche lobe, both Mg^+ lines should have been observed, given the assumed magnesium density profile. However, we do not consistently detect a significant magnesium signature in the data (greater than 3σ), at any of the considered resolving powers, neither from Mg nor Mg^+.

Our analysis supports the detection of many individual lines (Figure 3). The best match occurs between 2325 and 2420 Å, where the observed spectrum shows robustly detected absorption features at the location of a dozen of strong Fe^+ lines. However, the match is not perfect, as there are a few strong Fe^+ lines without a detected counterpart. More puzzling is that the data does not show robustly detected features at 2600 Å, where there is another complex of Fe^+ lines that are as strong as those at 2400 Å. Interestingly, the WASP-121b NUV transmission spectrum reported by Sing et al. (2019), observed with the same instrument and detector, also shows a similar trend. There are numerous other observed absorption features that are too weak to claim a detection ($S/N < 3\sigma$), or are not consistently detected at multiple shifts.

Certainly, better calculations of the density profiles, extending beyond the Roche lobe, are required to constrain the physical conditions of the upper atmosphere and escape. Even with these limitations, however, the model demonstrates that the magnitude of the detected Fe^+ transit depths is consistent with escape models for the atmosphere of HD 209458b, provided that iron is not removed from the upper atmosphere by condensation (see, e.g., Lavvas et al. 2014). This case is similar to that of WASP-121, where, if the NUV excess absorption is real, it is most likely caused by Fe^+ (Salz et al. 2019).

5.1. Comparison with Vidal-Madjar et al. (2013)

Our analysis benefits from advances in data analysis that the transiting-exoplanet community has experienced over the past decade. In particular, we applied techniques that were not available or widely used in the field at the time of Vidal-Madjar et al. (2013), which allowed us to analyze this data set in new light. In the first place, the divide-white analysis offers an alternative route to extract the wavelength-dependent transit depths (as opposed to the AD(λ) method). Second, the Bayesian MCMC analysis allowed us to estimate more robust transit-depth uncertainties. Lastly, the wavelength calibration of the significant radial-velocity shifts over time and wavelength might have an impact on the results as well. Given these different approaches, and other low-level details in the data analysis, it can be expected that our results differ from those of Vidal-Madjar et al. (2013).

Interestingly, our conclusions for the broadband analysis agree well with those of Vidal-Madjar et al. (2013), both finding a baseline transit depth of 1.44% ($R_p/R_s \sim 0.12$), where the first two *HST* visits agree with each other, and the third visit presents much stronger systematics (in flux as well as in wavelength calibration).

Regarding the high-resolution analysis of the spectral features, the detection of the Mg absorption feature by Vidal-Madjar et al. (2013), absent in our re-analysis, remains the main discrepancy. Although we do find excess-absorption features at transit-depth levels of ~6% ($R_p/R_s \sim 0.24$) around the location of the Mg line (see Figure 5), these are not significant at the 3σ level (consistent with the 2.1σ result of Vidal-Madjar et al. 2013). Our further exploration of the NUV transmission spectrum allowed us to identify a series of data points with increased absorption deviating more than 3σ above the continuum, where many of them could be associated to Fe^+ line transitions.

5.2. Broader Impact: Connection to Lower Atmosphere and FUV Observations

Although our results resolve the tension given by the previous detection of Mg and nondetection of Mg^+, in principle, they pose a new challenge. Lower-atmosphere modeling of HD 209458b indicate that iron and magnesium-bearing cloud condensation

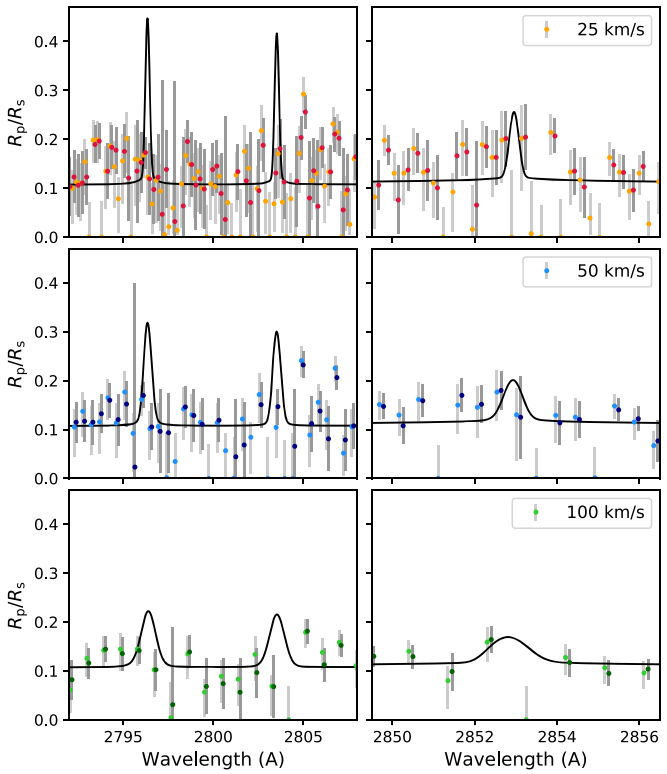

Figure 5. HD 209458b transmission spectrum around the Mg^+ *h* and *k* (left) and Mg (right) resonance lines at three of the four considered resolving powers (see the legend). The light and dark colored dots denote the transit depths obtained from the light-curve fit and AD methods, respectively. The AD results are shifted horizontally for visibility. The light and dark gray vertical lines denote the 68% highest-posterior density credible region of the light-curve fit and the uncertainties of the AD methods, respectively. The black solid lines show the magnesium absorption profiles based on the densities in Figure 4 uncapped at the Roche lobe boundary (unlike in Figure 3). This theoretical spectrum has been convolved to the resolution given in the legend. None of the different analyses detect consistently any significant absorption feature at the wavelength of the magnesium lines.

curves lie close enough to each other that if Mg condenses into clouds, then Fe should also condense (e.g., Lavvas et al. 2014), in direct contrast with our results. Recently, using an aerosol microphysics model to directly compute nucleation and condensation rates, Gao et al. (submitted) find that magnesium-silicate clouds dominate the aerosol opacity at planetary equilibrium temperatures of HD 209458b. The higher nucleation energy barrier of iron condensates prevents significant amounts of iron cloud formation, compared to magnesium-silicates, even though there is as much iron as silicon or magnesium available in the atmosphere. Therefore, this microphysics model offers a theoretical framework consistent with our results.

In relationship to the FUV observations, Shaikhislamov et al. (2020) performed 3D hydrodynamic simulations of the upper atmosphere and circumplanetary environment of HD 209458b. They obtained that to fit the 8% FUV transit-depth absorption by Si^{2+} observed by Linsky et al. (2010), they need to decrease the silicon abundance to nearly 10 times smaller than solar. Assuming that the clouds are composed mostly of enstatite ($MgSiO_3$) or forsterite (Mg_2SiO_4), there would be at least as much magnesium as silicon locked into condensates. Hence, with a magnesium abundance of 0.1 times solar, they estimate a magnesium transit-depth absorption of only 2%, which is compatible with the (nondetection) observations presented here.

6. Conclusions

We re-analyzed the NUV transmission spectroscopy observations of HD 209458b presented by Vidal-Madjar et al. (2013), making use of the improved knowledge and experience in handing systematic noise gathered in recent years in the exoplanet community. The detection of Mg and nondetection of Mg^+ presented by Vidal-Madjar et al. (2013) posed a challenge to the exoplanet atmospheric modeling community, which could not be solved simply by considering Mg recombination (see also Shaikhislamov et al. 2018 for a discussion on this topic). Furthermore, theoretical models predict the presence of a large number of metallic transition lines in the NUV spectrum. These considerations led us to this re-analysis.

We employed a two-step analysis: first, identifying the instrumental systematics from the wavelength-integrated light curves; and then, extracting the wavelength-dependent transmission spectrum from the systematics-corrected light curves. We implemented two independent spectral analyses, leading to comparable results. Our transmission spectra indicate the presence of absorption features extending beyond the Roche-lobe boundary at wavelengths below ∼2500 Å, with the strongest absorption concentrating around ∼2400 Å. A probabilistic line-identification approach (Haswell et al. 2012), and direct comparisons to theoretical models indicate that the detected absorption features are most probably caused by Fe^+ line transitions. This requires iron atoms to be lifted beyond the planet's Roche lobe; for example, entrained in the hydrodynamic expansion of the atmosphere by collisions with hydrogen atoms (e.g., Koskinen et al. 2014). We also find no robust evidence of either Mg or Mg^+ absorption in the planetary upper atmosphere, though, if present at the same altitudes as Fe^+, the data would enable us to detect it. There are plausible absorption features around the Mg^+ *h* line; however, the data shows no companion features at a similar shift around the equally strong Mg^+ *k* line. In agreement with Vidal-Madjar et al. (2013), we find that the NUV continuum absorption is consistent with Rayleigh scattering.

Line broadening from natural and Doppler broadening (FWHM of $\sim 3\,km\,s^{-1}$), planetary rotational velocity ($2\,km\,s^{-1}$), wind velocities ($2\,km\,s^{-1}$; Snellen et al. 2010), and escape velocity ($1–10\,km\,s^{-1}$; Koskinen et al. 2013a) is small compared to the spectral bin size of $25\,km\,s^{-1}$ adopted in our analysis. However, the radial component of the planet's orbital velocity changes from the beginning to the end of the transit by $\sim 30\,km\,s^{-1}$ (Snellen et al. 2010), which can make the absorption features to appear weaker in the analysis. By repeating the spectral light-curve fitting at multiple sub-bin shifts ($5\,km\,s^{-1}$), we mitigate ill-posed scenarios where a line might fall near the edge of a bin. We will directly account for the orbital radial-velocity shift in a future study using the high-resolution cross-correlation technique (in preparation).

By not finding any robust detection of magnesium in the upper atmosphere, our results resolve the conundrum presented by Vidal-Madjar et al. (2013). Furthermore, recent state-of-the-art microphysics models suggest that cloud formation can largely favor the formation of magnesium (and therefore, sequestering) over iron condensates in the lower atmosphere, providing a plausible theoretical interpretation of our results.

The upper-atmosphere models that we employed are based on an appropriate hydrodynamic framework and chemical network, but they adopt a 1D parameterization of the atmosphere, thus

limiting our capability to use the observations to firmly constrain the physical conditions of the upper atmosphere and escape. More complex models, accounting for all relevant physical effects (e.g., the 3D dynamics that the material follow beyond the Roche-lobe boundary) are required to best exploit the already available and future observations.

Previous (Vidal-Madjar et al. 2013) and our own analysis of the observed NUV transmission spectrum of HD 209458b have revealed challenges to upper-atmosphere models, as well as results from lower-atmosphere observations. Having the possibility to observe both the upper and lower atmosphere of an exoplanet highlights the value of a holistic characterization of exoplanet atmospheres. This and other contemporary NUV studies (e.g., Sing et al. 2019) show that this is possible.

The close-in orbit, large radius, and bright host star of HD 209458b give this planet a pivotal role for exoplanet atmospheric characterization. Few other planets will ever enable such precise measurements of their upper- and lower-atmosphere properties. Thus, a better understanding of the upper atmosphere of this important target would prove to be particularly useful, especially before the imminent launch of the *James Webb Space Telescope*. While we robustly detected several absorption features matching Fe^+ transition lines on HD 209458b (at a $S/N > 3\sigma$), there are many other weaker features in the spectrum. If the features that we see are of astrophysical nature, further NUV observations could potentially uncover from dozens to hundreds of additional Fe and Fe^+ features, and place stronger constraints to the strength of the Mg and Mg^+ lines (if present at all). Data of the necessary quality could only be currently obtained with *HST*.

A dedicated mission for UV spectroscopic observations, such as the Colorado Ultraviolet Transit Experiment (CUTE; Fleming et al. 2018), is therefore an efficient way to collect NUV observations to prove or disprove the presence of magnesium in the upper atmosphere. The combined CUTE and *HST* data will enable a firm interpretation of the results, and provide solid constraints to lower and upper atmosphere modeling.

This work demonstrates the need for comparative analyses of archival data sets with full transparency and for repeated observations of the same target aiming at improving data quality, transit light-curve coverage, and robustness of the results against instrumental and astrophysical noise.

We thank the anonymous referee for their time and valuable comments. We thank Peter Gao and Ildar Shaikhislamov for valuable discussions that helped to place our results in a broader context. We thank contributors to the Python Programming Language and the free and open-source community (see Software section below). This research has made use of NASA's Astrophysics Data System Bibliographic Services. We drafted this article using the AASTeX6.2 latex template (AAS Journals Team & Hendrickson 2018), with further style modifications available at https://github.com/pcubillos/ApJtemplate. A.G.S. and L.F. acknowledge financial support from the FFG projects 859718 and 865968. M.E.Y. and L.F. acknowledge funding from the "Innovationfonds Forschung, Wissenschaft und Gesellschaft" project of the Austrian Academy of Sciences entitled "Toward Extra-Terrestrial Habitats (TETH)." C.A.H. gratefully acknowledges financial support from STFC under grant ST/P000584/1. Based on observations made with the NASA/ESA *Hubble Space Telescope*, obtained at the Space Telescope Science Institute, which is operated by the Association of Universities for Research in Astronomy, Inc., under NASA contract NAS 5-26555. These observations are associated with program #11576.

Software: MC3[8] (Cubillos et al. 2017), Limb-darkening[9] (Espinoza & Jordán 2015), CLOUDY (Ferland et al. 2017), NUMPY (van der Walt et al. 2011), SCIPY (Jones et al. 2001), MATPLOTLIB (Hunter 2007), ASTROPY (Astropy Collaboration et al. 2013), IPYTHON (Perez & Granger 2007), AASTeX6.2 (AAS Journals Team & Hendrickson 2018), ApJtemplate (https://github.com/pcubillos/ApJtemplate), and BIBMANAGER[10] (Cubillos 2019).

Appendix
Supplementary Figures

Figure 6 shows the order-by order white-light curves and their best-fitting transit model. Figure 7 compares sample order-integrated light curves with and without the ramp systematic correction.

[8] https://github.com/pcubillos/mc3
[9] https://github.com/nespinoza/limb-darkening
[10] https://pcubillos.github.io/bibmanager

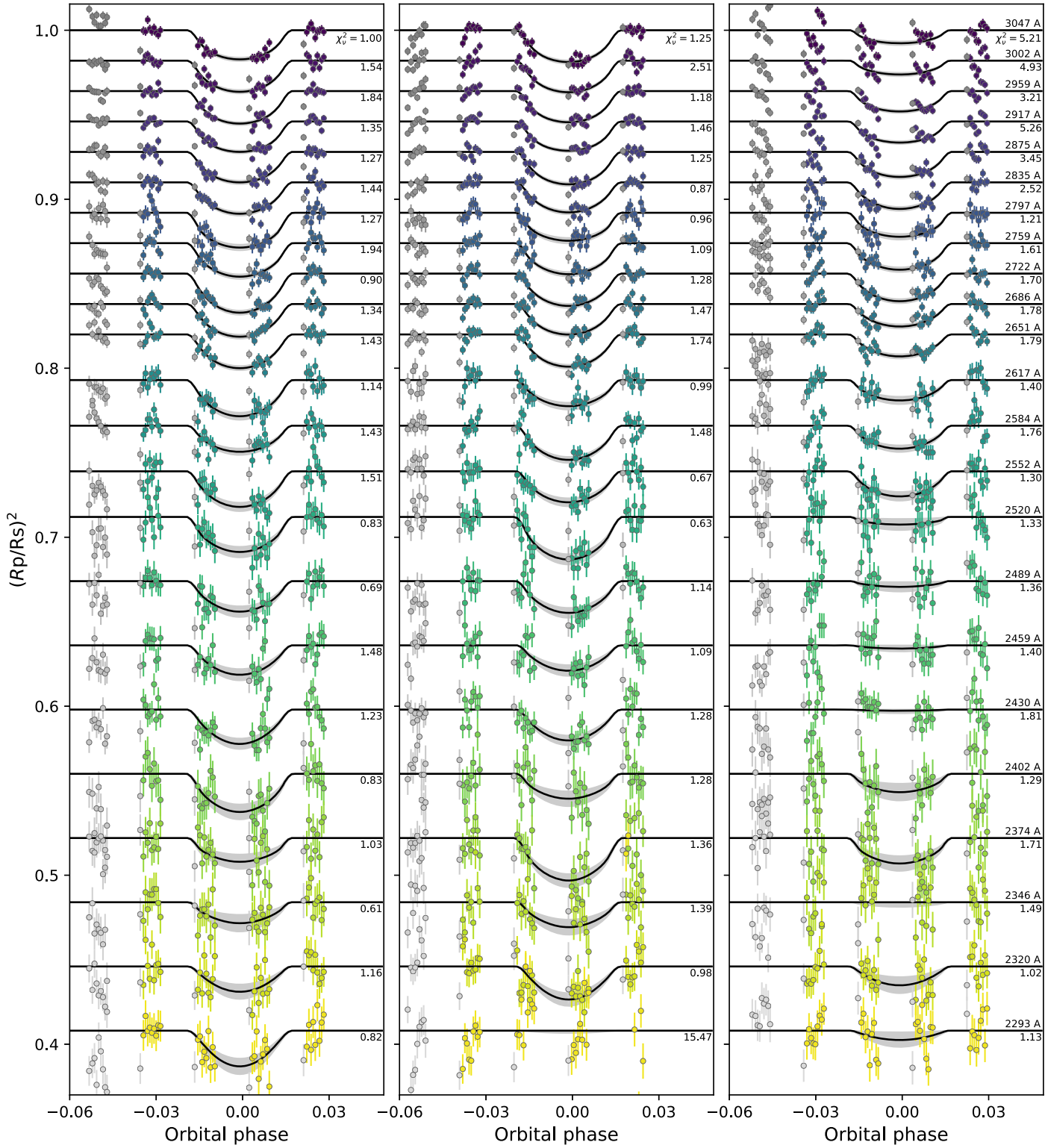

Figure 6. Light-curve observations (markers with error bars) and best-fit model (black curves) for each visit (left to right panels) and spectral order (top to bottom curves). The shaded gray areas denote the span of models for the 0.68-quantile from the MCMC posterior distribution. The numbers below each model show the reduced chi-squared (χ^2_ν) for each light curve. The numbers above each model on the right panel show the central wavelength of each spectral order.

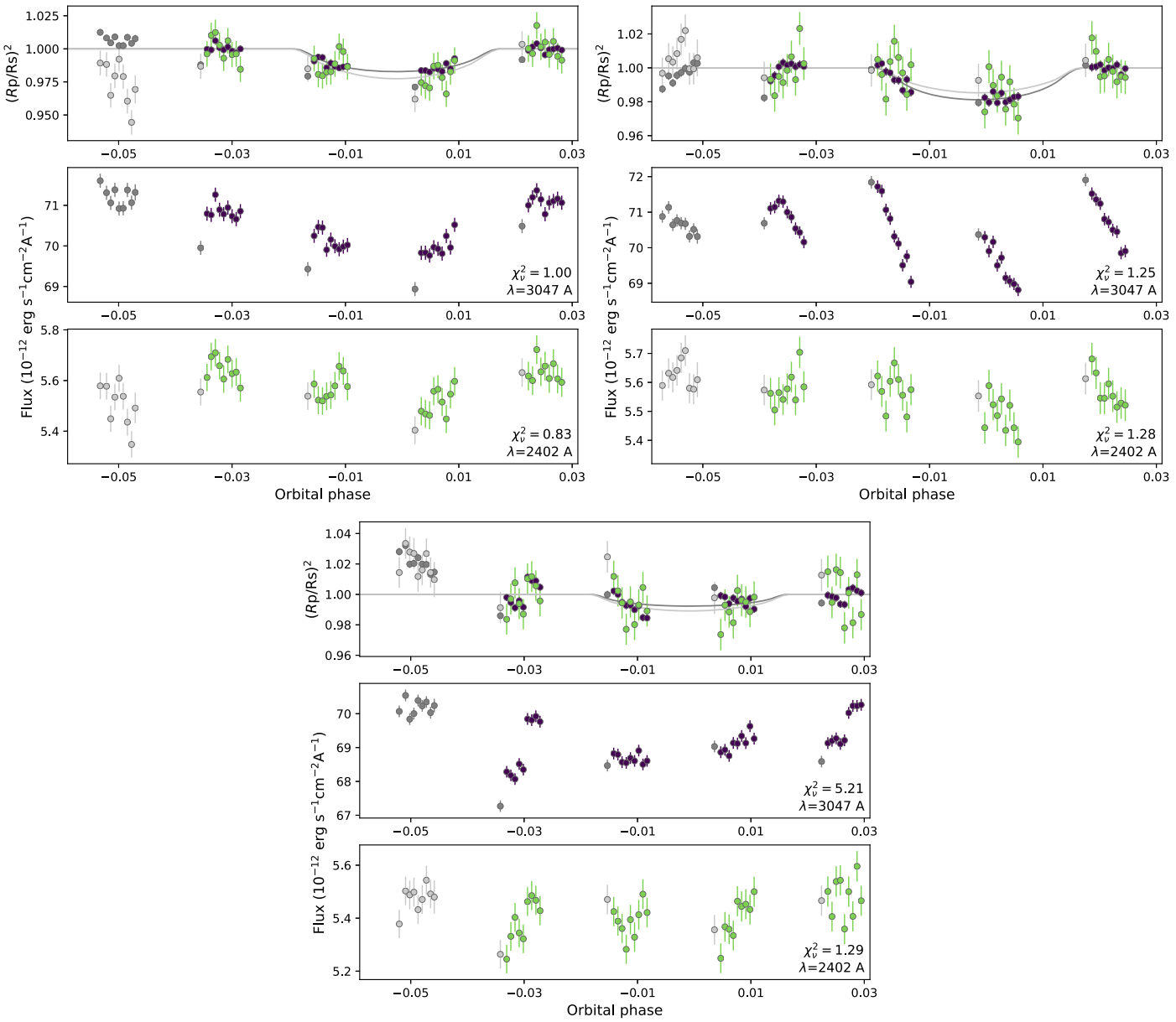

Figure 7. Sample order-integrated light curves for visit 1 (top left set of panels), visit 2 (top right set of panels), and visit 3 (bottom set of panels). For each visit, the top panel shows the systematics-corrected light curve for the first (λ = 3047 A, dark colors) and 19th (λ = 2402 A, light colors) order, whereas the middle and bottom panels show the raw integrated-flux light curves for the first and 19th orders, respectively.

ORCID iDs

Patricio E. Cubillos https://orcid.org/0000-0002-1347-2600
Luca Fossati https://orcid.org/0000-0003-4426-9530
Mitchell E. Young https://orcid.org/0000-0003-0672-7123
Kevin France https://orcid.org/0000-0002-1002-3674

References

AAS Journals Team, & Hendrickson, A. 2018, Aasjournals/Aastex60: Version 6.2 Official Release, doi:10.5281/zenodo.1209290
Alam, M. K., Nikolov, N., López-Morales, M., et al. 2018, AJ, 156, 298
Asplund, M., Grevesse, N., Sauval, A. J., & Scott, P. 2009, ARA&A, 47, 481
Astropy Collaboration et al., Robitaille, T. P., Tollerud, E. J., et al. 2013, A&A, 558, A33
Ballester, G. E., & Ben-Jaffel, L. 2015, ApJ, 804, 116
Ben-Jaffel, L. 2007, ApJL, 671, L61
Bevington, P. R., & Robinson, D. K. 2003, Data Reduction and Error Analysis for the Physical Sciences (3rd Ed.; Boston, MA: McGraw-Hill)
Bourrier, V., & Lecavelier des Etangs, A. 2013, A&A, 557, A124
Bourrier, V., Lecavelier des Etangs, A., Ehrenreich, D., et al. 2018, A&A, 620, A147
Bourrier, V., Lecavelier des Etangs, A., & Vidal-Madjar, A. 2014, A&A, 565, A105
Bourrier, V., Lecavelier des Etangs, A., & Vidal-Madjar, A. 2015, A&A, 573, A11
Carroll-Nellenback, J., Frank, A., Liu, B., Quillen, A. C., Blackman, E. G., & Dobbs-Dixon, I. 2017, MNRAS, 466, 2458
Charbonneau, D., Brown, T. M., Latham, D. W., & Mayor, M. 2000, ApJL, 529, L45
Charbonneau, D., Brown, T. M., Noyes, R. W., & Gilliland, R. L. 2002, ApJ, 568, 377
Claret, A. 2000, A&A, 363, 1081
Cubillos, P. 2019, bibmanager: A BibTeX manager for LaTeX projects, Version 1.2.0, Zenodo, doi:10.5281/zenodo.2547042
Cubillos, P., Harrington, J., Loredo, T. J., et al. 2017, AJ, 153, 3
Debrecht, A., Carroll-Nellenback, J., Frank, A., et al. 2018, MNRAS, 478, 2592
Deming, D., Wilkins, A., McCullough, P., et al. 2013, ApJ, 774, 95

Edwards, B., Mugnai, L., Tinetti, G., Pascale, E., & Sarkar, S. 2019, AJ, 157, 242
Ehrenreich, D., Bourrier, V., Wheatley, P. J., et al. 2015, Natur, 522, 459
Espinoza, N., & Jordán, A. 2015, MNRAS, 450, 1879
Evans, T. M., Sing, D. K., Goyal, J. M., et al. 2018, AJ, 156, 283
Ferland, G. J., Chatzikos, M., Guzmán, F., et al. 2017, RMxAA, 53, 385
Fleming, B. T., France, K., Nell, N., et al. 2018, JATIS, 4, 014004
Fossati, L., Haswell, C. A., Froning, C. S., et al. 2010, ApJL, 714, L222
Fossati, L., Haswell, C. A., Linsky, J. L., & Kislyakova, K. G. 2015, in Characterizing Stellar and Exoplanetary Environments, ed. H. Lammer & M. Khodachenko (Berlin: Springer), 59
France, K., Stocke, J. T., Yang, H., et al. 2010, ApJ, 712, 1277
Gaia Collaboration, Brown, A. G. A., Vallenari, A., et al. 2018, A&A, 616, A1
García Muñoz, A. 2007, P&SS, 55, 1426
Haswell, C. A. 2010, Transiting Exoplanets (Cambridge: Cambridge Univ. Press)
Haswell, C. A. 2018, in Handbook of Exoplanets, ed. H. J. Deeg & J. A. Belmonte (Cham: Springer), 97
Haswell, C. A., Fossati, L., Ayres, T., et al. 2012, ApJ, 760, 79
Hayek, W., Sing, D., Pont, F., & Asplund, M. 2012, A&A, 539, A102
Hunter, J. D. 2007, CSE, 9, 90
Jones, E., Oliphant, T., Peterson, P., et al. 2001, SciPy: Open Source Scientific Tools for Python, http://www.scipy.org/
Khodachenko, M. L., Shaikhislamov, I. F., Lammer, H., et al. 2017, ApJ, 847, 126
Kislyakova, K. G., Holmström, M., Lammer, H., Odert, P., & Khodachenko, M. L. 2014, Sci, 346, 981
Knutson, H. A., Charbonneau, D., Noyes, R. W., Brown, T. M., & Gilliland, R. L. 2007, ApJ, 655, 564
Koskinen, T. T., Harris, M. J., Yelle, R. V., & Lavvas, P. 2013a, Icar, 226, 1678
Koskinen, T. T., Yelle, R. V., Harris, M. J., & Lavvas, P. 2013b, Icar, 226, 1695
Koskinen, T. T., Yelle, R. V., Lavvas, P., & Y-K. Cho, J. 2014, ApJ, 796, 16
Kreidberg, L., Bean, J. L., Désert, J.- M., et al. 2014, Natur, 505, 69
Kubyshkina, D., Fossati, L., Erkaev, N. V., et al. 2018, ApJL, 866, L18
Lammer, H., Selsis, F., Ribas, I., et al. 2003, ApJL, 598, L121
Lavvas, P., Koskinen, T., & Yelle, R. V. 2014, ApJ, 796, 15
Lecavelier des Etangs, A., Bourrier, V., Wheatley, P. J., et al. 2012, A&A, 543, L4
Linsky, J. L., Yang, H., France, K., et al. 2010, ApJ, 717, 1291
Llama, J., & Shkolnik, E. L. 2015, ApJ, 802, 41
Llama, J., & Shkolnik, E. L. 2016, ApJ, 817, 81
MacDonald, R. J., & Madhusudhan, N. 2017, MNRAS, 469, 1979
Madhusudhan, N., Crouzet, N., McCullough, P. R., Deming, D., & Hedges, C. 2014, ApJL, 791, L9
Mandel, K., & Agol, E. 2002, ApJL, 580, L171
Murray-Clay, R. A., Chiang, E. I., & Murray, N. 2009, ApJ, 693, 23
Perez, F., & Granger, B. E. 2007, CSE, 9, 21
Pinhas, A., Madhusudhan, N., Gandhi, S., & MacDonald, R. 2019, MNRAS, 482, 1485
Piskunov, N. E., Kupka, F., Ryabchikova, T. A., Weiss, W. W., & Jeffery, C. S. 1995, A&AS, 112, 525
Plane, J. M. C., Feng, W., & Dawkins, E. C. M. 2015, ChRv, 115, 4497
Salz, M., Schneider, P. C., Czesla, S., & Schmitt, J. H. M. M. 2015, A&A, 576, A42
Salz, M., Schneider, P. C., Fossati, L., et al. 2019, A&A, 623, A57
Shaikhislamov, I. F., Khodachenko, M. L., Lammer, H., et al. 2018, ApJ, 866, 47
Shaikhislamov, I. F., Khodachenko, M. L., Lammer, H., et al. 2020, MNRAS, 491, 3435
Showman, A. P., Fortney, J. J., Lian, Y., et al. 2009, ApJ, 699, 564
Shulyak, D., Tsymbal, V., Ryabchikova, T., Stütz, C., & Weiss, W. W. 2004, A&A, 428, 993
Sing, D. K., Fortney, J. J., Nikolov, N., et al. 2016, Natur, 529, 59
Sing, D. K., Lavvas, P., Ballester, G. E., et al. 2019, AJ, 158, 91
Snellen, I. A. G., de Kok, R. J., de Mooij, E. J. W., & Albrecht, S. 2010, Natur, 465, 1049
Spake, J. J., Sing, D. K., Evans, T. M., et al. 2018, Natur, 557, 68
ter Braak, C. J. F., & Vrugt, J. A. 2008, Statistics and Computing, 18, 435
van der Walt, S., Colbert, S. C., & Varoquaux, G. 2011, CSE, 13, 22
Vidal-Madjar, A., Désert, J. M., Lecavelier des Etangs, A., et al. 2004, ApJL, 604, L69
Vidal-Madjar, A., Huitson, C. M., Bourrier, V., et al. 2013, A&A, 560, A54
Vidal-Madjar, A., Lecavelier des Etangs, A., Désert, J. M., et al. 2003, Natur, 422, 143
Vidal-Madjar, A., Lecavelier des Etangs, A., Désert, J. M., et al. 2008, ApJL, 676, L57
Wakeford, H. R., Sing, D. K., Evans, T., Deming, D., & Mandell, A. 2016, ApJ, 819, 10
Yelle, R. V. 2004, Icar, 170, 167